Journal of Computational Physics **149,** 293–305 (1999)
Article ID jcph.1998.6154, available online at http://www.idealibrary.com on IDEAL®

Time-Domain Deconvolution Removes the Effects of Near-Field Scatterers

Thomas M. Roberts

Air Force Research Laboratory/SNHA, 31 Grenier Street, Hanscom Air Force Base, Massachusetts 01731
E-mail: tmr@zippy.rl.plh.af.mil

Received May 28, 1998; revised October 22, 1998

This paper studies deconvolution algorithms for removing the interference caused by objects near an antenna. Infinitely many time-domain algorithms are considered, the best of which may compete with frequency-domain methods. Special care is taken to find a stable deconvolution algorithm that also accommodates the discontinuity-related numerical noise in standard finite-difference time-domain data.

Key Words: Time-domain; deconvolution; near-field; scattering; diffraction; Volterra; pulse; antenna; interference; FDTD; finite difference; electromagnetic; compute; numerical; transients.

1. INTRODUCTION

This paper studies the removal of electromagnetic interference produced by near-field scatterers. The numerical examples will roughly represent the removal of interference caused by a mast, wing tip, or fin that is near a ship or airborne receiving antenna [1–3].

The above-described work will be seen, in Section 3, to reduce to the deconvolution of the right-hand side of (1) below. This deconvolution could easily be done using Fourier [4] or Laplace transforms. This paper's goal, therefore, is to find what may be the best alternative time-domain algorithm. The best time-domain algorithm here will feed one-degree-smoothed data into a first-kind Volterra equation solver [5] that is stable and second-order accurate, and for which Richardson extrapolation yields fourth-order accuracy. This algorithm will also accommodate the discontinuity-related numerical noise in finite-difference time-domain (FD) data. These properties make the time-domain algorithm competitive with frequency-domain methods [4].

The central equation of the preferred algorithm will be shown, in Section 3, to be

$$\int_0^t R(s)\,\mathrm{d}s = \int_0^t K_{\mathrm{H}}(t-s)\,f_{\mathrm{inc}}(s)\,\mathrm{d}s, \tag{1}$$

0021-9991/99 $30.00

where R is the signal received after a nearby scatterer interferes with an incident signal f_{inc}. The identity (1) follows directly from the Duhamel theorem [6] about the Heaviside-step responses K_{H} of time-dependent linear systems, such as the Maxwell equations. The discontinuous kernel K_{H} will be computed here using a standard FD (finite-difference time-domain) method, despite the numerical noise resulting from the discontinuity. This approach arose from an earlier observation [7] that the standard-FD propagation of discontinuities is useful for linear scattering. This paper and [7] are complementary in that the central operator of [7] is a convolution and the central operator here is the deconvolution of (1).

Two prototype problems are defined in Section 2. Section 3 examines an infinite sequence of time-domain algorithms, each of which could solve the prototype problems. The section also finds the one algorithm of the sequence that has the best numerical properties. Section 4 numerically solves the prototype problems of Section 2 using the chosen algorithm. The conclusion (Section 5) describes the relation of the present work to [7], which together have two uses for the standard-FD propagation of discontinuous functions. Finally, the Appendix discusses more-realistic problems.

2. TWO PROTOTYPE PROBLEMS

This section's prototype problems will be solved numerically in later sections. These problems involve the parameters of an existing antenna [8], sketched in Figs. 1 and 2. This section will define the problems and say what they represent.

There is initially, for $t < 0$, no field in the rectangular domain of Fig. 1. At $t = 0$, a time-dependent field becomes incident uniformly from the right. The electric component of that field is always perpendicular to the page. The field represents a pulse that

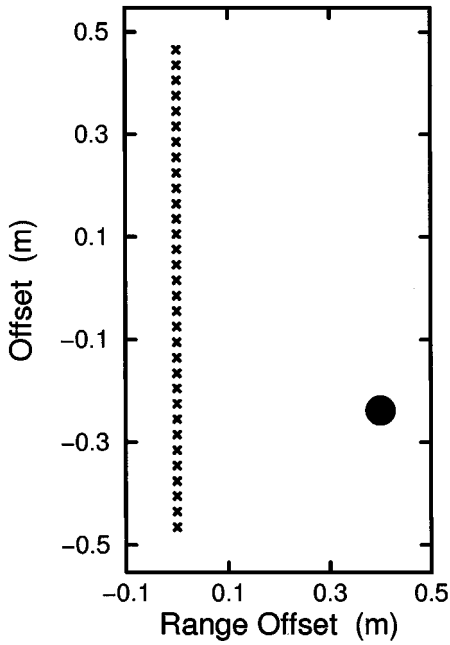

FIG. 1. Scale drawing of a steel disk and the 32 locations (×) where the total field is received inside the computational domain.

is incident from a source that is far from the scatterer. The word "far" conventionally [3] refers to a distance of at least, say, 10 times L^2/λ, where L is the larger of the diameters of the scatterer and antenna, and λ is a wavelength typical of the incident field. The incident field propagates through free space ($\varepsilon = \varepsilon_0$ and $\mu = \mu_0$) and scatters from an insusceptible ($\mu = \mu_0$) conducting ($\sigma \leq \infty$) object. The scattering object of the first prototype problem is the disk of Fig. 1. The total time-dependent electric field is measured at each $\times$-marked location in the figure, and it is assumed that the measurements do not perturb the field. This electric field is the subject of all equations and graphs in this paper.

Let $R_j(t)$ be the field measured at the jth $\times$-marked location from the bottom of Fig. 1. Then this paper's prototype problems are as follows: Given the total field R_j at a single known location, knowing that R_j was produced by a plane-wave pulse incident from a known direction, and knowing also the location, shape, and composition (ε and σ) of the scatterer, one must compute the time trace of the incident pulse f_{inc}.

The first prototype problem roughly represents the removal of the electromagnetic interference from a mast, wing tip, or fin that is near $[\leq L^2/(10\lambda)]$ a ship or an airborne antenna [1, 2]. In Section 4 the incident pulse is a 1-cycle sinusoid with a 5.45-GHz carrier frequency, whose free-space wavelength is approximately the diameter of the steel disk of Fig. 1. Because the wavelength is also about the length of two $\times$-marked intervals in Fig. 1, this problem represents an existing 32-element phased-array radar antenna [8] that has a wavelength-sized steel pipe located 40 cm in front of it. That pipe adds interference, which deconvolution will remove.

The second prototype problem has multiple scattering, although only between the components of a scatterer, drawn in Fig. 2. All parts of this problem are the same as those for Fig. 1, except for the scatterers. Notice that the misaligned ellipses of Fig. 2 add asymmetry

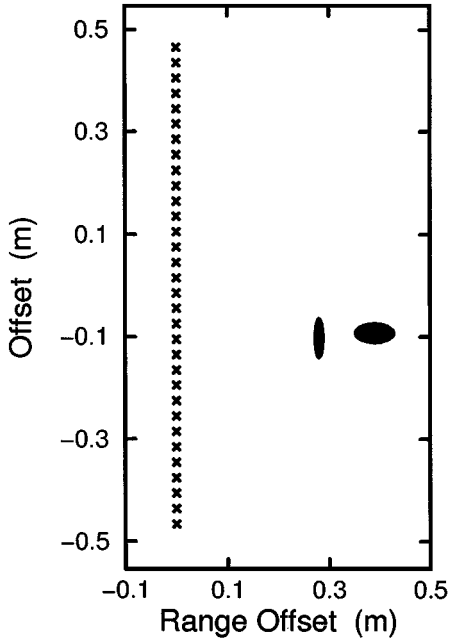

FIG. 2. Scale drawing of a two-ellipse scatterer that produces multiple scattering.

to this problem. The ellipses will also be seen to prolong some received signals or cause ringing. These multiple-scattering effects will be removed by deconvolution in Section 4.

The Appendix illustrates the stability of deconvolution under large errors in incident direction. The Appendix also discusses multiple scattering among the antenna elements ($\times$ marks of Figs. 1 and 2), and the use of laboratory data.

3. NUMERICAL METHODS AND THEIR PROPERTIES

The deconvolution problems of Section 2 are linear; therefore, they can be solved in the frequency domain [4]. This section will consider infinitely many time-domain alternatives (3), and will examine their numerical properties to find the best one (3b).

Linear time-domain systems, such as the Maxwell equations, can usually be described by the Duhamel theorem [6], which is the basis for this paper's work. This paragraph will sketch a verification that the Duhamel theorem does apply here. Then the theorem will be used. To begin: The problems of Section 2 are described by the Maxwell equations $\nabla \cdot D = \nabla \cdot B = \nabla \times E + \partial_t B = \nabla \times H - \partial_t D - J = 0$ and the constitutive relations $D = \varepsilon E,\ J = \sigma E,$ and $B = \mu_0 H$. The parameters ε and σ are functions in the x–y plane, but μ_0 is a constant. All three parameters are independent of t. The only nonzero electric component of the field of the two-dimensional problems of Section 2 therefore satisfies

$$\partial_x^2 E + \partial_y^2 E = \mu_0 \partial_t (\varepsilon \partial_t E + \sigma E). \tag{2}$$

An existing proof [6] of the Duhamel theorem is then easily modified to accommodate the $\partial_y^2 E$ term of (2). To connect that proof with the present work, however, the antenna and its nearby scatterer are both located near $l/2$ in the notation of [6], where l is exceedingly large. The Duhamel theorem then applies rigorously to the problems of Section 2.

The Duhamel theorem and its immediate generalizations yield infinitely many integral equations for sufficiently smooth incident fields f_{inc}. The equations are

$$R(t) = \int_0^t K_\delta(t-s)\, f_{\text{inc}}(s)\, \mathrm{d}s \tag{3a}$$

$$\partial_t^{-1} R(t) = \int_0^t K_{\text{H}}(t-s)\, f_{\text{inc}}(s)\, \mathrm{d}s \tag{3b}$$

$$\partial_t^{-2} R(t) = \int_0^t K_{t\text{H}}(t-s)\, f_{\text{inc}}(s)\, \mathrm{d}s, \tag{3c}$$

$$\vdots \qquad\qquad \vdots$$

where ∂_t^{-2} is the antiderivative operator $\partial_t^{-1} R(t) \equiv \int_0^t R(s)\, \mathrm{d}s$ composed with itself. The kernels of (3) denote the delta-function response, K_δ, the Heaviside response, K_{H}, and the ramp-function $[t\text{H}(t)]$ response, $K_{t\text{H}}$, at the location where a received signal R is measured. The phrase "delta-function response" above refers to the response of (2) to an incident field that is a Dirac delta function. For linear hyperbolic systems, such as the time-domain Maxwell equations, a propagation-of-singularities argument [6] shows that K_δ itself has a delta-function component. However, [7] shows that a bounded (L_∞) approximation of δ can be propagated usefully using standard FD. If K_δ of (3a) is computed using such an L_∞

approximation, then the entire sequence (3a), (3b), (3c), ... is of first-kind Volterra integral equations (for f_{inc}) with convolution kernels.

We now consider a numerical property that will help us identify the best algorithm in (3): Linz [5] showed that if the left-hand side of a general first-kind Volterra equation

$$L(t) = \int_0^t K(t,s)\, f(s)\, \mathrm{d}s \tag{4}$$

is perturbed by an amount ΔL, then the resulting perturbation of the solution of (4) is, in what is probably the best case,

$$\Delta f = O(h^{-1}\Delta L). \tag{5}$$

That ill-posedness result (5) favors equations that have smooth left-hand sides. Consequently, (3a) is not the best algorithm of (3).

We still have infinitely many algorithms—(3b), (3c), ...—the best of which will be found only after a method for solving first-kind equations is described. This method will be described as it applies to the eventually preferred algorithm (3b), but the same method can be easily modified for all algorithms in (3).

Direct methods for solving first-kind equations (4) follow immediately from discretization of the integral. The midpoint-rule discretization of (3b) yields

$$f_1 = \frac{\left[\partial_t^{-1} R\right]_1}{\left[h K_{\text{H}}\left(\frac{h}{2}\right)\right]} \tag{6a}$$

$$f_n = \frac{1}{\left[h K_{\text{H}}\left(\frac{h}{2}\right)\right]} \left(\left[\partial_t^{-1} R\right]_n - h \sum_{i=1}^{n-1} K_{\text{H},n-i}\, f_i \right), \tag{6b}$$

where

$$f_n = f_{\text{inc}}\left[\left(n - \tfrac{1}{2}\right)h\right] \tag{7a}$$

$$K_{\text{H},n} = K_{\text{H}}\left[\left(n - \tfrac{1}{2}\right)h\right] \tag{7b}$$

$$\left[\partial_t^{-1} R\right]_n = \int_0^{nh} R(s)\, \mathrm{d}s \tag{7c}$$

are stepsize-h discretizations. If

$$|hK_{\text{H}}(h/2)| \ll \min\left(|f_n|,\ \left|\left[\partial_t^{-1} R\right]_n\right|\right) \tag{8}$$

then the numerator of (6b) is a small difference of large numbers, and significant digits are thereby lost. Algorithm (3b) is therefore preferred because a propagation-of-singularities argument [6] shows that $K_{\text{H}}(0^+) \neq 0$, whereas the integral kernels of (3c), (3d), *et seq.* are continuous and zero at $t = 0$. (Their zeros are first order for $K_{t\text{H}}$, second order for $K_{t^2\text{H}}$, and so forth.) This issue has theoretical significance for the left-hand side of (8) and its generalizations for $K_{t\text{H}}$ and $K_{t^2\text{H}}$. In corroboration, numerical experiments have shown that the above-described loss of significant digits causes a rapid numerical blowup for the first-order-zero case (3c). Equation (3b) therefore yields the best of the infinitely many algorithms that follow from (3). (An imperfection of (3b) is studied in the last paragraph of Section 4.) The sentence that contains (8) also yields a rough lower bound on h: namely, there should be

at most a few time steps n at which $|hK_{\mathrm{H}}(h/2)|$ is much less than both $|f_n|$ and $|[\partial_t^{-1}R]_n|$. But clearly, h should also be significantly briefer than the time scales typical of $\partial_t^{-1}R$, K_{H}, and f. We therefore have approximate upper and lower bounds on the stepsize h.

The preferred algorithm (3b) will now be improved. Linz [5] has shown that the error of the midpoint-rule computation (6)–(7) is

$$f_{\mathrm{exact}} - f_n = \frac{h^2}{24}\varepsilon_n + O(h^4), \tag{9}$$

where ε_n is independent of h. This allows for Richardson extrapolation [5], yielding fourth-order accuracy. Equation (9) also shows that the computation (6)–(7) is stable as $h \to 0$. These useful properties are the reasons that the midpoint rule is used in (5)–(8) to select the best algorithm.

These are the numerical properties of the deconvolution algorithm (3b): The data R are first smoothed using integration in (3b). Equations (4) and (5) show that the algorithm's ill-posedness is thereby reduced. The smoothed data $\partial_t^{-1}R$ are fed into a routine (6) that is seen in (9) to be stable and second-order accurate. Richardson extrapolation, based on (9), then yields fourth-order accuracy. For any error tolerance, the $O(h^4)$ method allows a larger h to be used. A larger h will further reduce sensitivity to perturbations of the data, according to (5). It will also preserve significant digits, according to (8). But h should not be allowed to far exceed either bound described in the first three or four sentences before (9).

We turn now to purely computational issues. To begin, if the discontinuous kernel K_{H} of (3b) is computed with standard FD, then the computed K_{H} will include a large amount of purely numerical noise. We will briefly consider two alternatives to such a noisy computation of K_{H}; then, in the next paragraph, we will see how to easily overcome the noise. First, the numerical noise would be much smaller were K_{H} computed with an essentially non-oscillatory (ENO) method [9, 10]. The adaptive stencils of ENO methods do, however, make their results nonlinear, and perhaps inappropriate for the deconvolution of linear systems. Standard FD is used here instead of an ENO method for that reason. A second alternative to the standard-FD propagation of the discontinuous K_{H} is to propagate the ramp function $t\mathrm{H}(t)$ and then differentiate, as in $K_{\mathrm{H}}(\tau) = \partial_\tau K_{t\mathrm{H}}(\tau)$. But numerical noise would then be magnified by differentiation. The kernel K_{H} is therefore, for simplicity, computed directly by propagating $\mathrm{H}(t)$ using standard FD.

The numerical noise of K_{H} is easily overcome. When the grid properly resolves the scatterer, this noise will have a regular number of points per oscillation, 10 to 20 in the computations of Section 4. The results of those computations, therefore, are smoothed with a 40-point filter Φ

$$f \overset{\Phi}{\mapsto} \frac{1}{T_{\mathrm{M}} + t_{\mathrm{m}}} \int_{-t_{\mathrm{m}}}^{T_{\mathrm{M}}} f(t+s)\,\mathrm{d}s, \tag{10}$$

where $t_{\mathrm{m}} = 19h$, $T_{\mathrm{M}} = 20h$, and f is a generic function. That filter is also a convolution

$$\Phi * f = \int_{-\infty}^{\infty} \Phi(t-s)\, f(s)\,\mathrm{d}s \tag{11a}$$

$$\Phi(t) = (T_{\mathrm{M}} + t_{\mathrm{m}})^{-1}\mathrm{H}(t + t_{\mathrm{m}})\mathrm{H}(T_{\mathrm{M}} - t) \tag{11b}$$

for all $t \in (-\infty, \infty)$. The equation

$$\partial_t^{-1}(\Phi * R) = (\Phi * K_{\mathrm{H}}) * f_{\mathrm{inc}} \tag{12}$$

then follows from (3b) and elementary calculus [11]. That equation is an identity. But the next, and final, computational issue will lead to an approximation of (3b) and (12).

The wavefront of an FD-computed pulse travels with the superluminal velocity c/CFL because of the nature of time stepping in a CFL-stabilized computation. The filtered pulses $(\Phi * R)$ and $(\Phi * K_{\mathrm{H}})$ are therefore truncated as

$$(\Phi * K_{\mathrm{H}}) \overset{\mathcal{T}}{\mapsto} (\Phi * K_{\mathrm{H}})\mathrm{H}(t) \tag{13a}$$

$$(\Phi * R) \overset{\mathcal{T}}{\mapsto} (\Phi * R)\mathrm{H}(t), \tag{13b}$$

where t is now measured relative to the analytically determined wavefront-arrival time of each receiver. (That arrival time is the same for all receivers of Figs. 1 and 2. For more complicated media, the arrival time can be computed using characteristics or the eikonal equation [6].) The quantities on the right-hand sides of (13a) and (13b) replace, respectively, K_{H} and R in (6). Notice that the truncation of the superluminal FD-computed K_{H} assures that the right-hand side of (13a) will be discontinuous at $t = 0$. This is beneficial according to (8). It may also be the only known computational advantage of the superluminal feature of CFL-stabilized FD. If, however, K_{H} were known exactly by analytical means then a propagation-of-singularities argument [6] would prove that K_{H} already is discontinuous. Regardless of whether K_{H} is computed exactly or with filtered-then-truncated FD, its discontinuity at $t = 0$ will yield the numerical benefits described by (5) and (8).

The main disadvantage of truncation (13) is its approximation to what would otherwise be an identity (9). It has been proven [11], however, that the truncation errors of (13) vanish as $h \to 0$, provided the superluminal parts of the FD-computed R and K_{H} tend to 0 pointwise as $h \to 0$.

4. NUMERICAL SOLUTIONS

This paper's prototype problems are defined in Section 2. The incident fields are one-cycle 5.45-GHz sinusoidal pulses. That frequency is the midpoint of the frequency range of the existing antenna [8] modeled here by these problems. The corresponding wavelength is 5.5 cm, which can be compared in Fig. 1 with the 3-cm element ($\times$ symbol) spacing and the 6-cm disk diameter. The steel disk has a conductivity of 10^7 S/m and its permittivity is that of free space. The remainder of Fig. 1 has free-space properties.

Fields were computed with a standard-FD program that was written [12] in accordance with an early manuscript version of [13], but whose absorbing boundary condition was replaced [12] with a Berenger PML [14]. The FD program computed electric fields that were always perpendicular to the plane of Fig. 1. The program was second-order accurate in space and time. It was run with $\mathrm{CFL} = 1/2$ on a 2840×5232 spatial grid, yielding 4735 points per carrier-frequency period. This grid was used to compute the one-cycle-sinusoid responses $R_j(t)$ of Fig. 3, and to compute K_{H}.

Figure 3 shows the signals $R_2(t)$, $R_4(t)$, $\ldots$, $R_{32}(t)$ that are received at every other location in Fig. 1. These signals are vertically offset in Fig. 3. The largest and smallest offsets are used, respectively, for the top and next-to-bottom $\times$-marked locations in Fig. 1. The steel disk casts a shadow whose darkest part is R_{10} of Fig. 3. Note also the delayed-wave components of the signals.

The integral kernel K_{H} and each received signal R_j were filtered, truncated, and time shifted as in (10)–(13). The results were fed into the second-order-accurate routine (6)–(7).

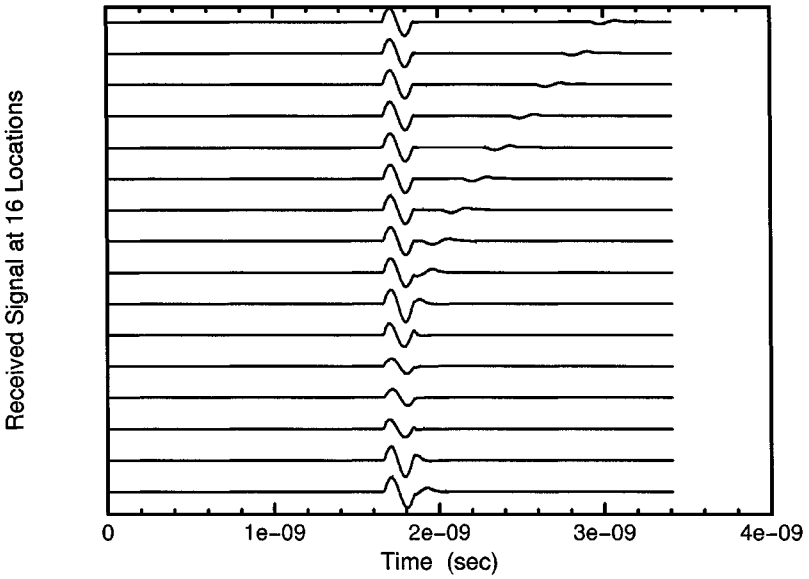

FIG. 3. Total signal received at every other ×-marked location in Fig. 1.

Each received signal was deconvolved separately from the 31 other signals, resulting in 32 independent reconstructions of the incident field f_{inc}. Figure 4 shows a typical $O(h^2)$ reconstruction. This uses the signal received at the 15th × from the bottom of Fig. 1. The incident signal and its reconstruction almost overlap.

Figure 5 shows that each of the 32 second-order-accurate reconstructions of f_{inc} (curve with circles) reproduces the L_∞ norm of the one-cycle sinusoid f_{inc} (boldface line) within 2%. The L_2 norm (not graphed), whose square is proportional to the energy of a pulse, is reproduced to within 1.3%.

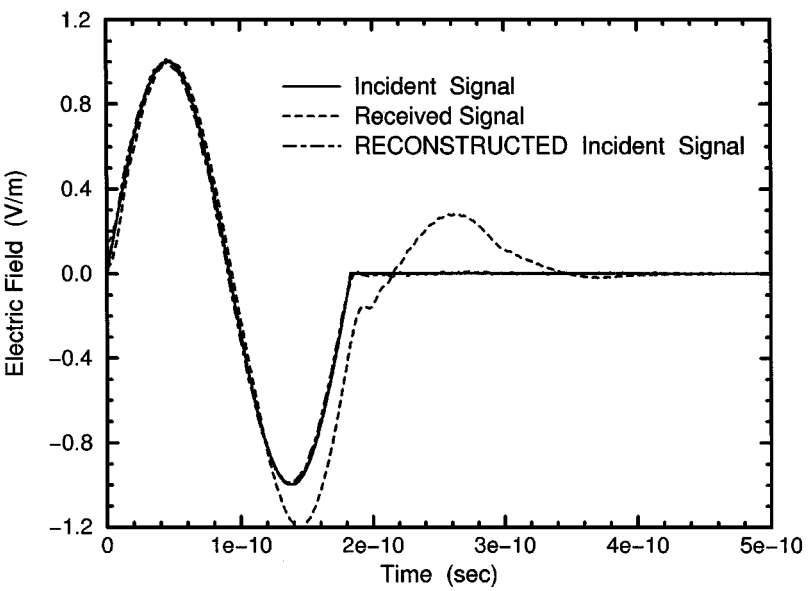

FIG. 4. Reconstruction of the incident signal f_{inc}, using one received signal from Fig. 1.

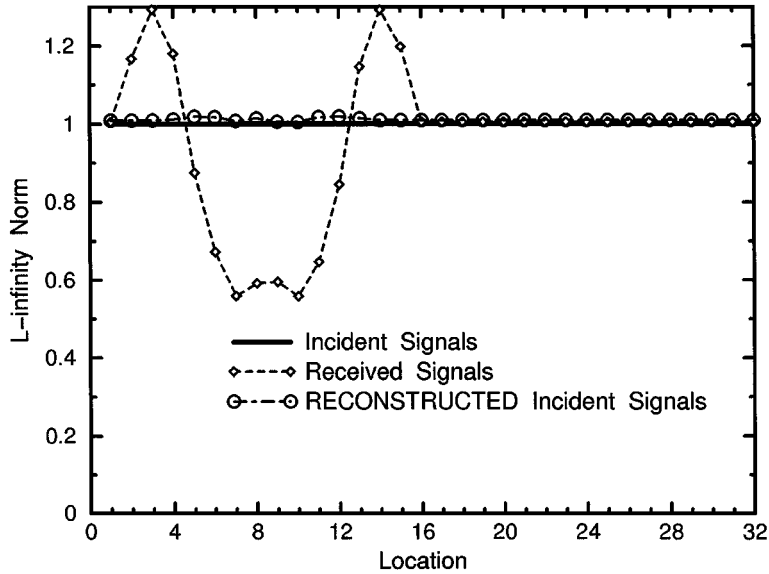

FIG. 5. Restoration of the L_∞ norm for all 32 locations in Fig. 1.

The predominant errors of these $O(h^2)$ results are barely evident in the figures. To find the predominant reconstruction error in Fig. 4, look along the left-hand vertical axis for a brief, diagonal segment near 0.15 V/m. That segment is difficult to find. The predominant errors of all 31 other $O(h^2)$ reconstructions also are difficult to find in their graphs (not presented). Richardson extrapolation [5] did further reduce the barely evident numerical errors of all 32 reconstructions.

The computations just described for the disk of Fig. 1 were redone for the two-ellipse scatterer of Fig. 2. Figures 6 and 7 show, respectively, the reconstructions for the 12th

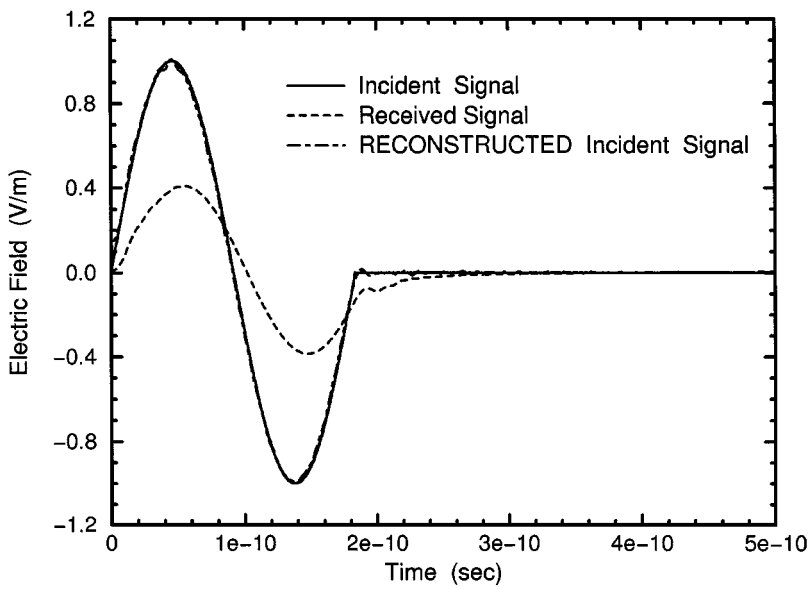

FIG. 6. Reconstruction of the incident signal f_{inc}, using a received signal from Fig. 2.

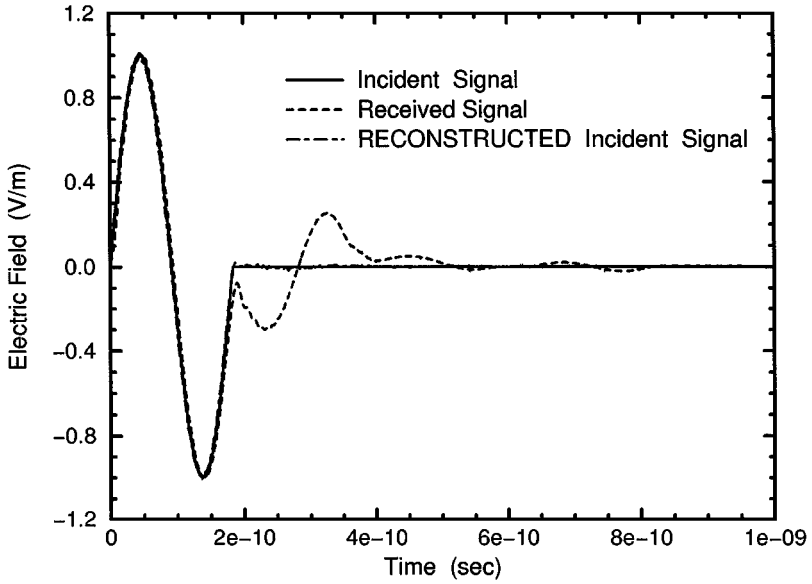

FIG. 7. Reconstruction of the incident signal f_{inc}, using a multiply scattered signal from Fig. 2.

and 21st $\times$-marked locations from the bottom of Fig. 2. Those locations were chosen because their received signals illustrate prolongation (Fig. 6) and ringing (Fig. 7) caused by multiple scattering. The incident and reconstructed signals almost overlap in Figs. 6 and 7. The predominant errors of 31 of the 32 second-order-accurate reconstructions are again confined to the first few data points and are barely evident in the graphs. Thus, time-domain deconvolution has removed the multiple-scattering effects of the two-ellipse scatterers in 31 of 32 cases. The single exception will now be studied.

The only failed reconstruction is for the 13th $\times$ from the bottom of Fig. 2 (two ellipses). That one reconstruction (not graphed) oscillates with exponentially increasing amplitude, as is typical of an unstable computation. The instability is evidently caused by lost significant digits, associated with condition (8). In particular, $|hK_{\text{H}}(h/2)|/\min(|f|, |\partial_t^{-1}R|)$ is 2.7% in this computation at the time (1.37×10^{-11} s) when divergence first becomes apparent at the 13th $\times$. That quotient is no less than 7.2% at the same time in the 31 convergent reconstructions for Fig. 2. That concludes the numerical evidence that (8) describes the one failure. Therefore, if it were crucial to have a convergent reconstruction based on the signal received at the 13th $\times$ from the bottom of Fig. 2, then (8) suggests that a larger h should be tried in (6)–(7). In any case, the 63 other reconstructions for Figs. 1 and 2 were successful.

5. CONCLUSION

This paper arose from [7]. There, the Kronecker-delta-function response K_δ was computed with standard FD and then used in (3a) to propagate other incident fields f_{inc}. Other reference pulses were considered as alternatives to K_δ, but [7] concluded that K_δ was the simplest reference pulse to use. Thus, K_δ and (3a) are best for the (convolutional) forward-propagation problem of [7], and K_{H} and (3b) are best for the (deconvolutional) reconstruction problem of the present paper. These two methods, (3a) and (3b), are useful

despite the fact that their integral kernels are standard-FD responses to discontinuous incident pulses. The time-domain-deconvolution method (3b) is, furthermore, stable and $O(h^2)$ accurate—it is $O(h^4)$ accurate after Richardson extrapolation—and it consequently may compete with frequency-domain methods [4].

The purely numerical noise in a computed Heaviside response K_H required a simple filter. The filtered result was also truncated to restore a discontinuity at $t = 0$ that tends to conserve significant digits (8). The filtering and truncation would have been unnecessary were K_H known exactly. The resulting algorithm yielded almost imperceptible errors in 63 of 64 cases. The exceptional case is evidently explained by (8), which also suggests a remedy.

The Appendix will discuss modifications for more-practical problems.

APPENDIX: GENERALIZATIONS

This appendix addresses three practical problems: First, the known angle of incidence may be in error. Second, the received signal may be affected by multiple scattering among antenna elements. Finally, one may want to use laboratory data.

We will start with errors in the angle of incidence. The sensitivity to these errors was tested by looking at received fields caused by 1-cycle sinusoids that were incident from 5° and 45° below the normal to the antenna of Fig. 1. The incident signals for 5° and 45° incidence were reconstructed using the K_H for 0° incidence, thereby introducing errors. All 64 reconstructions converged, with the $O(h^2)$ and $O(h^4)$ reconstructions practically indistinguishable. Figure 8 illustrates the three distinct types of reconstructed signals observed. The types involve prolongation, numerical noise, and ringing. The reconstructed signals do, of course, differ from the actual incident field because of the intentional errors in angle. For an arrangement other than Fig. 1, the effect of errors in angle would depend on the case

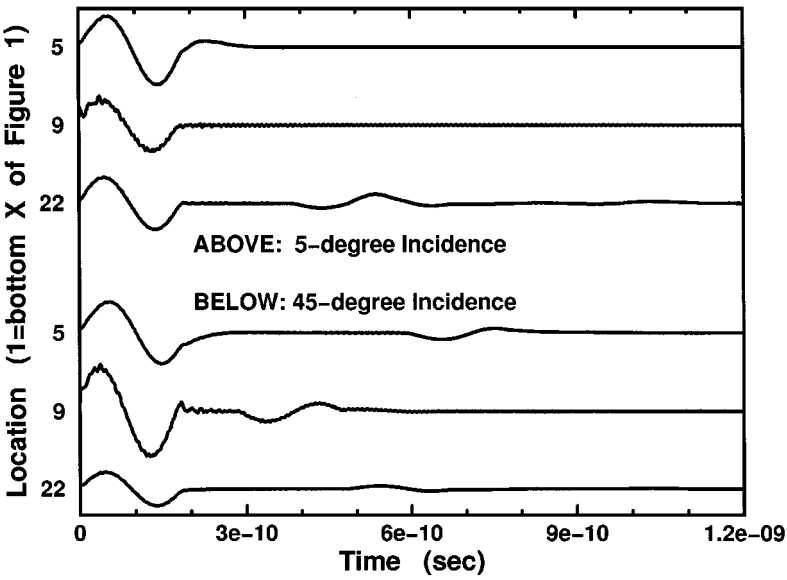

FIG. 8. Typical reconstructions of the one-cycle sinusoid f_{inc} when there are 5° and 45° errors in the angle of incidence.

at hand. Figure 8, however, illustrates stability under large errors. We now turn to multiple scattering.

The prototype problems' most idealized assumption is that the antenna measures the field nonperturbatively. This assumption neglects the important practical effect of multiple scattering among the 32 elements ($\times$ marks) of Figs. 1 and 2. One way to simulate multiple scattering would be to have an imperfect absorber in a small area near each $\times$-marked element, and perhaps a small conductor behind each imperfect absorber. In any case, the standard-FD response would still be a linear operator acting on the incident fields. The analysis in this paper would usually apply without change to any such linear system, including all that have multiple scattering.

We finally consider what could be done with laboratory data. Heaviside-step pulses are problematical in the laboratory, so it is likely that K_{H} would have to be inferred from other measurements. To remove interference in a frequency band $[\omega_{\min},\ \omega_{\mathrm{MAX}}]$, one would first propagate a physical reference pulse f_{ref} whose spectrum covers $[\omega_{\min}, \omega_{\mathrm{MAX}}]$ and whose risetime is $\ll 2\pi/\omega$. Or f_{ref} could be a suitable linear combination of narrow-band pulses. In either case, one would then solve (3b) numerically for K_{H} using the physical received signals R resulting from the known $f_{\mathrm{inc}} = f_{\mathrm{ref}}$. (The roles of K_{H} and f here are reversed from before.) If this K_{H} were truncated as in (13a), then the result could presumably be used as usual to reduce interference in the frequency band $[\omega_{\min},\ \omega_{\mathrm{MAX}}]$.

ACKNOWLEDGMENTS

This work was supported by the Air Force Office of Scientific Research. Peter G. Petropoulos allowed me to use his finite-difference program.

REFERENCES

1. H. Steyskal, Synthesis of antenna patterns with imposed near-field nulls, *Electron. Lett.* **30**, 2000–2001 (1994).
2. J. W. Fitton, Effects of near-field scatterers on space–time adaptive processing, Technical Report AFIT/GE/ENG/97D-12 (U.S. Air Force, 1997).
3. R. J. Mailloux, *Phased Array Antenna Handbook* (Artech House, Norwood, MA, 1994), p. 15.
4. W. L. Gans, The measurement and deconvolution of time jitter in equivalent-time waveform samplers, *IEEE Trans. Instrum. Measure.* **IM-32**, 126–133 (1983).
5. P. Linz, *Analytical and Numerical Methods for Volterra Equations* (SIAM, Philadelphia, 1985), Chap. 9.
6. R. Courant and D. Hilbert, *Methods of Mathematical Physics* (Interscience, New York, 1962), Vol. II, pp. 115–118, 416–421, 511–515, 620–635.
7. G. A. Kriegsman and J. H. C. Luke, Rapid pulse responses for scattering problems, *J. Comput. Phys.* **111**, 390–398 (1994).
8. L. Eber, Digital Beam Steering Antenna, Technical Report RADC-TR-88-83 (U.S. Air Force, 1988), Attachment 2.
9. A. Harten, B. Engquist, S. Osher, and S. R. Chakravarthy, Uniformly high order accurate essentially non-oscillatory schemes, III, *J. Comput. Phys.* **71**, 231–303 (1987), Abstract.
10. C.-W. Shu and S. Osher, Efficient implementation of essentially non-oscillatory shock-capturing schemes, II, *J. Comput. Phys.* **83**, 32–78 (1989), Introduction.
11. T. M. Roberts, Time-domain deconvolution removes the effects of near-field scatterers. Accepted as Technical Report AFRL-SN-RS-TR-1998-113 (U.S. Air Force, 1998), but not yet released. See the appendix of this reference.

12. P. G. Petropoulos, Department of Mathematics, New Jersey Institute of Technology, University Heights, NJ 07102 (personal communication, 1997).
13. A. Taflove, *Computational Electrodynamics: The Finite-Difference Time-Domain Method* (Artech House, Boston, 1995).
14. J.-P. Berenger, A perfectly matched layer for the absorption of electromagnetic waves, *J. Comput. Phys.* **114**, 185–200 (1994).